Babeș-Bolyai University

Faculty of Physics

Doctoral School of Physics

Summary of the PhD Thesis

Controlling the Plasmonic Nanoparticle-Molecule Interface
Through Adsorbed Ions

PhD student: Andrei Stefancu

Supervisor: Prof. Nicolae Leopold

Cluj-Napoca, 2021

Contents

Since the turn of the millennium, the interdisciplinary field of plasmonics has attracted the interest of scientists and engineers from different walks of life. The main reason behind this is the ability of plasmonic nanostructures to concentrate optical fields into volumes well below the diffraction limit, opening a plethora of potential applications in nanoscale systems, from detectors or sensors to optoelectronic devices or chemical catalysis.

The unifying feature of this thesis is the idea of modifying, in-situ, the chemical nature of the plasmonic metal-molecule interface through adsorbed ions (adions), such as halide ions or positively charged Mg^{2+} ions. Thus, we are able to investigate in real time the adsorption dynamic of different analytes for example, or the optical emission of molecules adsorbed at different metal-molecule interfaces. As I show throughout this thesis, the adions on the metal surface led to surprising effects, both for the plasmon-enhanced spectroscopy (such as SERS or SEF) and plasmonic catalysis (such as spontaneous charge transfer to adsorbed molecules or oxidative dissolution of metallic nanoparticles).

Introduction. Drude model and optical absorption by metal nanoparticles

In Chapter I, I introduce the basic theoretical aspects of optical absorption and emission by metals, which can be described by the Drude model. Next, I show both experimentally and theoretically how the surface plasmon resonance (SPR) of gold nanoparticles (AuNPs) is influenced by the refractive index of the surrounding medium, or, more interesting, by chemical interface damping (CID), which describes the scattering of the electrons participating in the plasmon resonance in surface adsorbate states. Moreover, in this Chapter, I introduce the idea of varying the charge density of metal nanoparticles through the adsorption of nucleophilic chemical species.

The dielectric constant of metallic nanoparticles describes the dispersive properties of nanoparticles and the interaction of metallic nanoparticles with light at different energies. The physical reason for this strong frequency dependence of the dielectric constant is a change in the

phase of the induced currents with respect to the driving field for frequencies approaching the reciprocal of the characteristic electron relaxation time of the metal. Mathematically, the dielectric constant is given by: [1]

$$\varepsilon_{Drude} = \varepsilon_\infty - \frac{\omega_p^2}{\omega^2 + i\gamma_b\omega} \qquad (1)$$

where ε_∞ is the core background polarization created by the ion core of the nanoparticles, γ_b is the damping of the bulk metal and ω_p is the plasma frequency of the metal, given by:[1]

$$\omega_p = \sqrt{\frac{Ne^2}{m^*\varepsilon_0}} \qquad (2)$$

where N is the free electron density, e is the elementary charge, m^* is the effective mass of charge carriers in the nanoparticles and ε_0 is the electric permittivity of free space.

In general, the dielectric constant is complex, the imaginary part describing the absorption of light. In Figure 1 we compare the real and imaginary part of the dielectric function of a 10 nm AuNP obtained from Drude model (equation (1)) with the experimental dielectric function from Johnson and Christy.

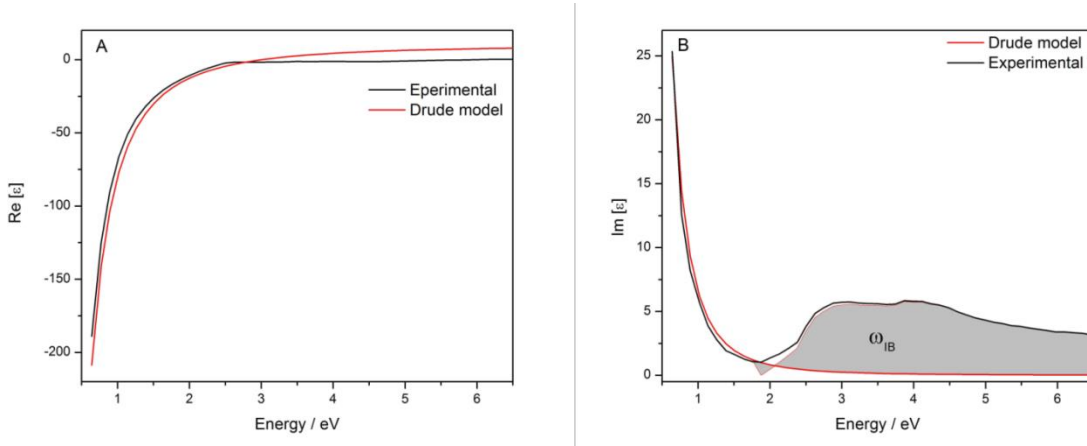**Figure 1.** Comparison of the real (A) and imaginary (B) parts of the dielectric constant of AuNPs obtained experimentally by Johnson and Christy[2] and simulated by us, based on the Drude model.

As can be observed, Drude model yields accurate results for the real part of dielectric constant. However, it does not take into consideration interband transitions, which in gold take place at

energies above 1.7 eV and contribute to the imaginary part of the dielectric constant, increasing the absorption. [1]

Up until now we used the *quasi-static* approximation which assumes that the nanoparticle is much smaller than the wavelength, such that the electromagnetic fields are constant over the entire volume of the metallic nanoparticles. However, for an accurate description of the optical response of metallic nanoparticles, retardation effects have to be taken into account, which appear due to the finite speed of light such that the electromagnetic fields are slightly different at different point inside nanoparticles. To take this effect into considerations, we need to solve the full Maxwell's equations for the metallic nanoparticles, which obviously adds to the computation time.

For simulating the retardation effects, we modified the diameter of the gold nanosphere between 5 and 75 nm and calculated the SPR energy for every diameter. In Figure 2 we present the resonance energy variation with increasing diameter, and compare these results with *quasi-static* results.
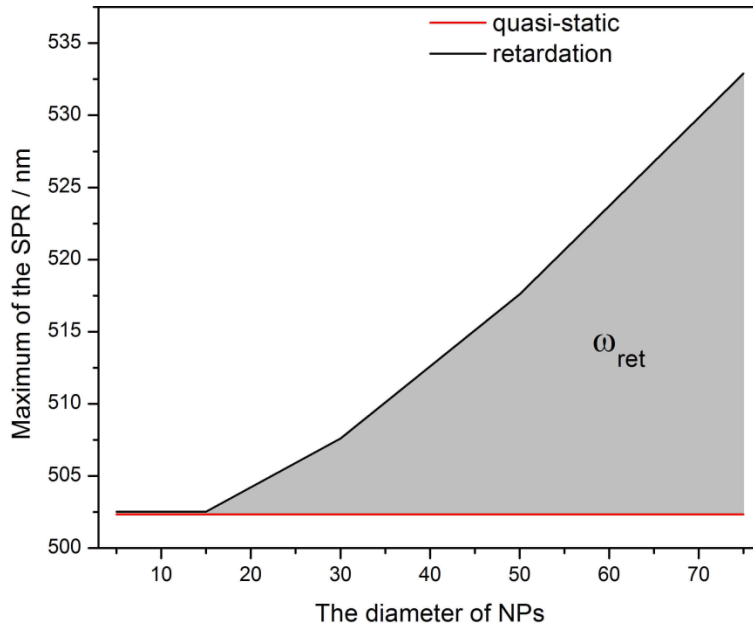

Figure 2. Retardation effects on the resonance energy of AuNPs which dependent on the diameter of the nanoparticles and represent the effect of the finite speed of light on the resonance energy.

Therefore, for a complete description of the optical response of AuNPs, we have to modify again the plasma frequency of AuNPs by adding an additional term representing retardation effects.

Influence of charge density

Naturally, nucleophilic molecules tend to donate an electron, so the chemisorption of nucleophilic molecules would result in the (partial) charge transfer from the adsorbed molecule to the nanoparticles. In order to see if this effect accounts in totality for the shift of the resonance energy upon $B(OH)_3$ chemisorption, we calculated the dielectric function of AuNPs using a modified charge density, ΔN, according to the following procedure:

$$\varepsilon_{\Delta N} = \varepsilon_{JC} - \varepsilon_{Drude}(\omega_p) + \varepsilon_{Drude}(\omega_{p'}) \qquad (3)$$

with

$$\omega_p = \sqrt{\frac{Ne^2}{m^*\varepsilon_0}} \qquad (4)$$

and

$$\omega_p' = \sqrt{\frac{(N+\Delta N)e^2}{m^*\varepsilon_0}} \qquad (5)$$

By introducing the extra term, ΔN in equation (5), we include the variation of charge density. Realistically, the charge density should not vary more than 1%, which happens if each adsorbed $B(OH)_3$ molecule donates one electron to the AuNP. In this case, the shift of the SPR energy is less than 2 nm (Figure 3). However, we varied ΔN from 0.5 to 3% to show the trend of the shift in SPR energy and simulated the resulting extinction spectra.
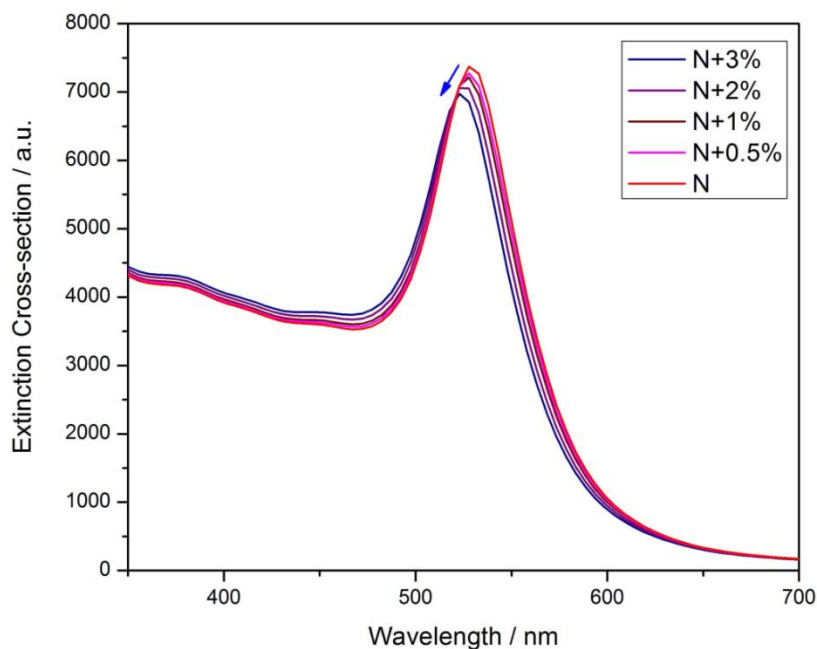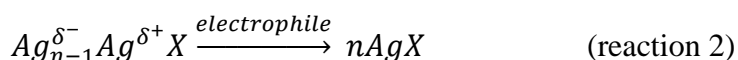
Figure 3. The SPR energy of AuNPs shifts towards higher energies following an increase in charge density. The shift of the SPR band was lower than 5 nm in the studied interval.

The blue shift of the SPR band can be explained based on the model proposed by Henglein *et al.* [3] They showed that adsorbed nucleophiles shift the Fermi level of AgNPs towards cathodic potentials, increasing the sensitivity of the nanoparticles for electrophilic molecules and leads to the oxidation of AgNPs by electrophilic molecules. For example, they reported the reduction of methyl viologen (MV^{2+}), which took place only after the surface of the nanoparticles was modified by nucleophilic species (CN^-). In the lack of the nucleophilic species, no interaction between MV^{2+} and AgNPs was observed. [3]

The chemisorption of nucleophiles onto AgNPs (which can also be used for AuNPs) can be modeled as follows:

$$Ag_nAg + X = Ag_{n-1}^{\delta^-}Ag^{\delta^+}X \qquad \text{(reaction 1)}$$

$$Ag_{n-1}^{\delta^-}Ag^{\delta^+}X \xrightarrow{electrophile} nAgX \qquad \text{(reaction 2)}$$
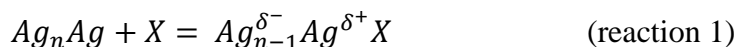
In the first step (reaction 1), a nucleophilic molecule donates an electron pair into an unoccupied orbital on the surface, the surface atom acquiring a slight positive charge δ^+ and the interior of the silver particle a corresponding negative charge δ^-. A certain number of surface atoms are

'pre-complexed' or 'pre-oxidized' this way until an equilibrium is reached where the negative charge accumulated inside prevents further electron donation.

In the second step (reaction 2), oxygen diffused in the colloidal solution picks up the excess negative charge of the interior and dissolves the metal as AgX molecules. These changes in the Fermi level of silver colloids are reflected as a shift on the SPR band of the gold colloid.

Influence of refractive index

To probe the effect of the change in refractive index of the embedding medium, we modeled a core-shell system. It is known from literature that $B(OH)_3$ molecules adsorb on metallic surfaces and form a thin layer with a thickness of approximately 1 nm. Since the refractive index of this adsorbed layer can change comparatively to isolated, free $B(OH)_3$ molecules, we varied the refractive index of the thin layer between 1.33 and 1.45 (Figure 4).
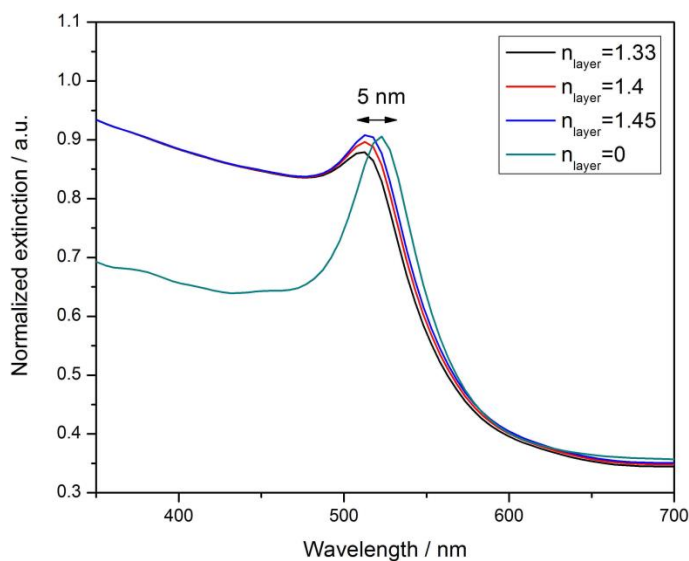
Figure 4. The effects of change in refractive index upon chemisorption, which leads to a damp of the SPR band, as well as the shift towards higher energies. The maximum shift of the SPR band is less than 5 nm.

As can be observed from the Figure 4, the SPR band shifts towards higher energies after the adsorption of $B(OH)_3$ due to the change in the surrounding medium. However, the shift observed was not higher than 5 nm in the studied interval.

We modeled two different physical systems presented schematically in Figure 5. We considered a gold sphere with diameter of 10 nm, unless otherwise stated. For simulating the change in refractive index determined by the adsorbed molecules, we created a core-shell system, with the core represented by a gold sphere with diameter of 10 nm and a coating layer of $B(OH)_3$ molecules with thickness of 1 nm and varying refractive index between 1.33 and 1.45.
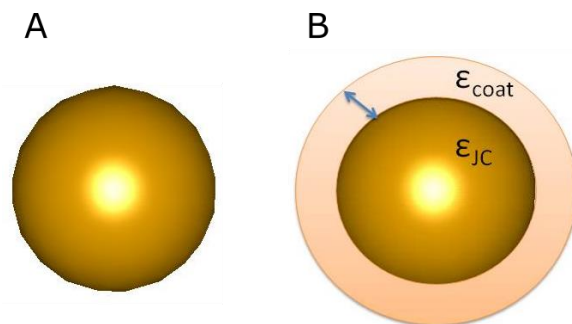
Figure 5. Schematic representation of the physical systems used for simulating the optical response of AuNPs. A: Gold nanosphere with diameter of 10 nm; B: Core–shell system with an inner core of gold with 10 nm diameter and an outer shell of thickness of 1 nm and refractive index determined by the specific chemical nature of the adsorbate. The representation is out of scale. ε_{JC} represents the dielectric function obtained experimentally by Johnson and Christy. [2]

Results and Discussion

Chapter II. The effect of adsorbed ions in metal nanoparticle dissolution

In **Chapter II**, I further extend the description of varying the charge density (and implicitly the Fermi level) of silver and gold nanoparticles through adsorbed iodide ions and investigate the catalyzed dissolution of metal nanoparticles due to repeated oxidative steps. Moreover, we show that by adding Mg^{2+} or Ca^{2+} ions, the adsorption of iodide is favored, resulting in an increased dissolution dynamic.

The dissolution of metallic NPs is closely linked to the chemisorption of strong nucleophiles such as I^-, SH^-, CN^- on the surface of the NPs through uncoordinated surface atoms and formation of surface complexes.[3]

Figure 6 shows schematically the mechanism of AuNPs dissolution after I⁻ chemisorption, as described in literature studies, with the mention that the mechanism can also apply to other metallic NPs such as AgNPs.
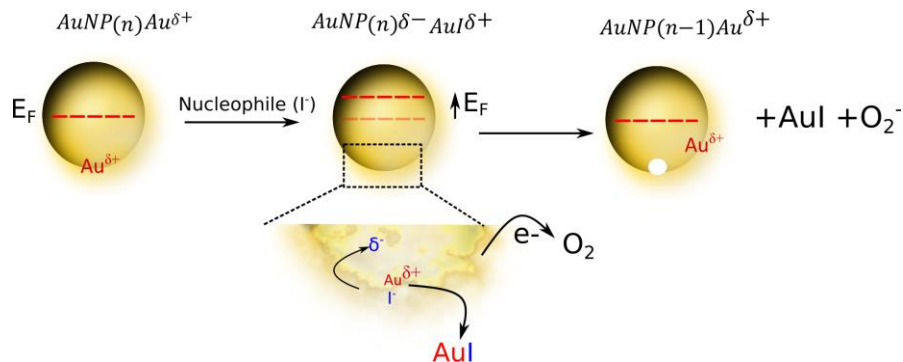

Figure 6. Schematic illustration of the mechanism of AuNP dissolution through electron density increase due to I⁻ chemisorption, followed by charge transfer to an oxygen molecule and subsequent release of a gold iodide complex into the bulk solution.

In the first step, I⁻ chemisorbs to the AuNP through an uncoordinated surface Au ion, forming a surface complex. Afterwards, a partial charge transfer from the chemisorbed I⁻ ion to the NP occurs, leaving the interior of the NP negatively charged. Due to the partial charge transfer to the metal, the Fermi energy (E_F) of the AuNP is raised to a higher energy and the NP becomes more reactive, i.e. more likely to be oxidized.

In the second step, electrophilic species, such as the oxygen molecule, can extract the extra charge from the NP, thus oxidizing the NP. Afterwards, the last step in the dissolution process consists in the separation of an Au^+I^- surface complex, which is solved into the bulk solution. Thus, through repeated oxidative processes, the NP is completely dissolved. The rate limiting step of the dissolution reaction is the chemisorption rate of I⁻.

The increase in electron density due to I⁻ chemisorption and subsequent oxidation and dissolution was monitored at single AuNP level by DFS, which allows the detection of the scattered light due to surface plasmon resonance (SPR), characteristic to plasmonic nanostructures. Figure 7 shows a typical dark-field image of AuNPs, drop-casted on a microscope slide, showing both individual AuNPs and AuNP aggregates.
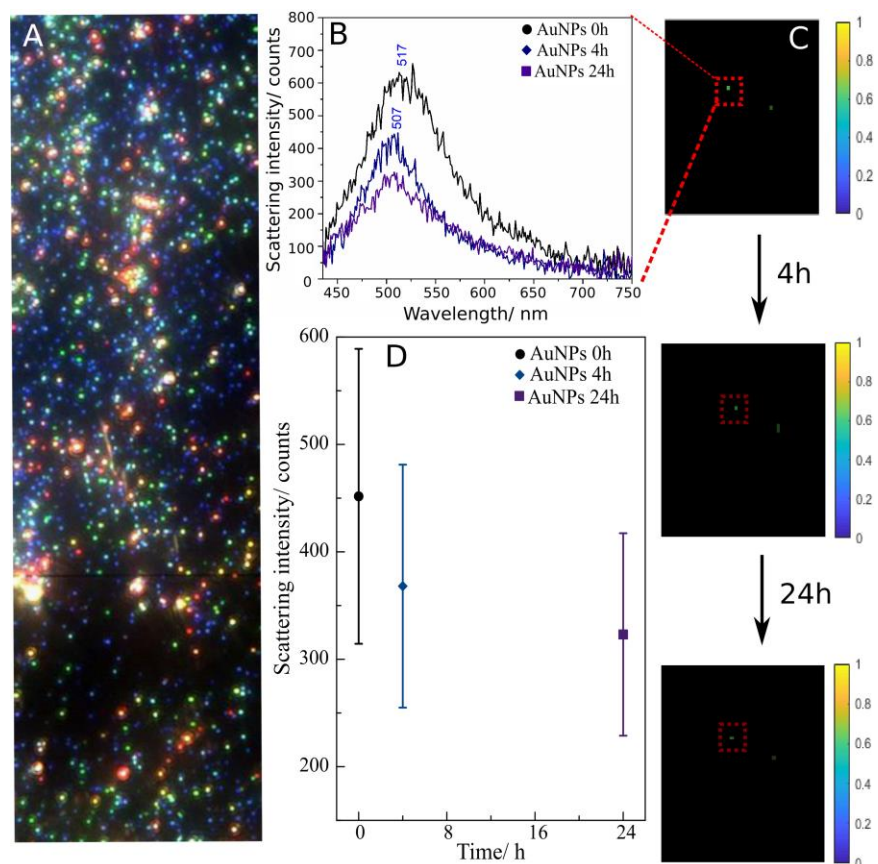
Figure 7. Electron density increase in AuNP due to I⁻ chemisorption and subsequent oxidation and dissolution, monitored through dark field spectroscopy (DFS) at single AuNP level. **(A)** A typical dark-field image of AuNPs, drop-casted on a microscope slide; **(B)** The scattering spectra of the particle shown in (C) at 0, 4 and 24 h after KI addition; **(C)** Representative dark field image of a single AuNP, showing a decrease of the scattering intensity in the timeframe 0–24 h; **(D)** Average and standard deviation of scattering intensity obtained from the same 20–30 isolated AuNPs at three timepoints after 10 mM KI (final concentration) addition, as mentioned in the inset.

Figure 7 depicts the dissolution of the single AuNP shown in Figure 7C, at 4 and 24 h after the addition of 10 mM KI (final concentration), tracked through the decrease and blue-shift of the scattering spectrum maximum intensity. The initial SPR spectrum of the single AuNP shows a peak at 517 nm, characteristic to a spherical AuNP with a diameter of 40–50 nm. Within 24 h after KI addition to the colloidal solution, the initial scattering intensity halves from

approximately 620 to 310 counts, and the maximum of the scattering spectrum appears blue-shifted by 10 nm; both effects indicate a decrease in the AuNP size.

Figure 7D depicts the average scattering intensity decrease in time due to the dissolution of the single AuNPs. The average scattering intensity of 20–30 single AuNPs decreases within 24 h by 30%, from 450 to 320 counts, due to the dissolution of the AuNPs in the presence of I^-. Although the colloidal AuNP solution drop casting can result in AuNPs aggregates (Figure 7A), leading to a polydisperse distribution and coupled SPR modes, we included only single, isolated particles (20 to 30 AuNPs) in our analysis. The SPR energy of these NPs was between 510–580 nm (corresponding to the green points in Figure 7A), characteristic to single, spherical AuNPs with a 40–80 nm diameter.

An increased dissolution rate of I^- modified colloidal AgNPs is observed when supplementing the solution with Mg^{2+}, as illustrated in Figure 8. The higher I^- chemisorption rate, due to additional surface adsorption sites promoted by Mg^{2+} adions, leads to a more significant partial charge transfer from chemisorbed I^- to the AgNP.

Since spherical AgNPs show a SPR band around 400 nm, we could not use DFS, which acquires the scattering spectra above 400 nm. Thus, we tracked the time-dependent dissolution of colloidal AgNPs by conventional UV-Vis spectroscopy.
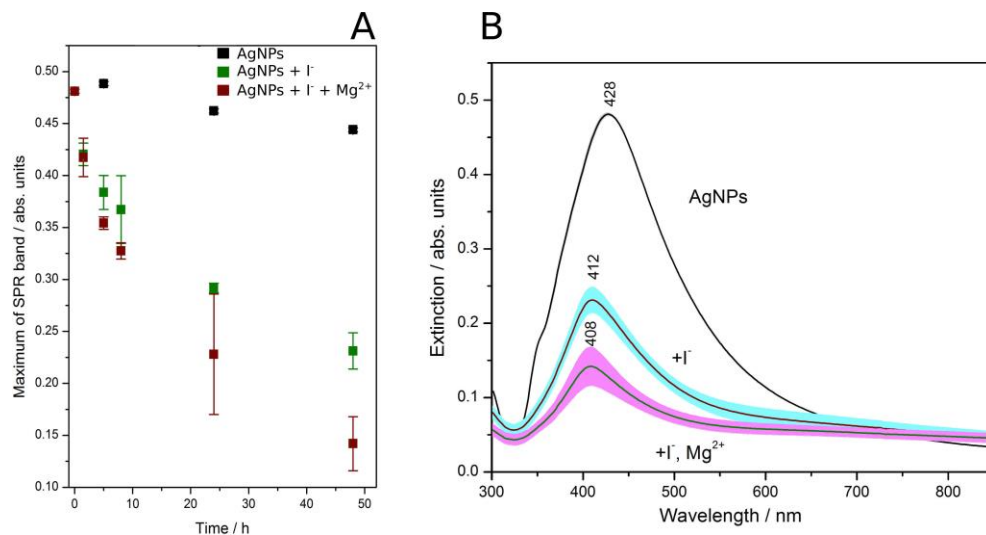

Figure 8. Dissolution of AgNPs in the presence of 10 mM I^-, and in the presence of 10 mM I^- and 0.1 mM Mg^{2+}. (**A**) Time-evolution of the SPR band of control AgNPs, AgNPs supplemented with I^- and AgNPs supplemented with I^- and Mg^{2+}. (**B**) Average extinction spectra of the

unmodified Ag colloid, of the colloidal AgNPs 48 h after supplementing with 10 mM I⁻, and of the colloidal AgNPs 48 h after supplementing with 10 mM I⁻ and 0.1 mM Mg^{2+}. Shadow area corresponds to standard deviation.

Figure 8A shows the dissolution of the AgNPs triggered by the adsorption of I⁻, monitored through the decrease in the SPR band intensity. For the as-synthesized Ag colloid, a slight decrease can be observed in the intensity of the SPR band in the timeframe of 48 h. In comparison, for the two colloidal solutions supplemented with 10 mM I⁻, and 10 mM I⁻ together with 0.1 mM Mg^{2+}, a significant blue-shift and decrease in the SPR band intensity can be observed in the timeframe of 48 h, evidencing the higher dissolution rate of AgNPs supplemented with I⁻ and Mg^{2+}.

This study on nanosurfaces can be extended to macroscopic surfaces with the aim to understand why corrosion of metals is more pronounced in natural aqueous media, especially in saline water, compared to air environments. Natural water contains a variety of cations and anions. Thus, cations such as Ca^{2+} or Mg^{2+} favor the chemisorption to the metal surface of nucleophiles such as Cl⁻, which increase the metal Fermi energy level. Natural occurring O_2 is then able to accept an electron from the metal; subsequently, a metal cation from the metal surface is released into the bulk solution, as described in this study. Thus, the dissolution of the metal occurs via such repetitive oxidative processes.

Chapter III. The effect of adsorbed ions on single molecule SERS (SM-SERS)

The idea of using adions to control the adsorption of positively and negatively charged analytes is further investigated in **Chapter III**, by SERS, at the single particle level. We show that from a mixture of positively and negatively charged analytes (rhodamine 6g and rose bengal respectively), the positively charged molecule adsorbs to the surface of silver nanoparticles only after the addition of Cl⁻ ions, whereas the negatively charged analyte (rose bengal), adsorbs only after the addition of Mg^{2+} or Ca^{2+}. From the best knowledge of the authors, this is the first report of single molecule SERS without the addition of Cl⁻ or Br⁻, in the case of rose bengal (where Ca^{2+} or Mg^{2+} was added).

The SERS spectra at "bulk" concentration (100 nM) for R6G and RB model analytes, taken with a 5X magnification objective (Leica, NA 0.12), are shown in Figure 9. For obtaining the SERS spectra of R6G, the citrate-capped AgNP colloid was activated with NaCl (1 mM), whereas RB adsorbed to the metal surface spontaneously at a concentration of 100 nM.
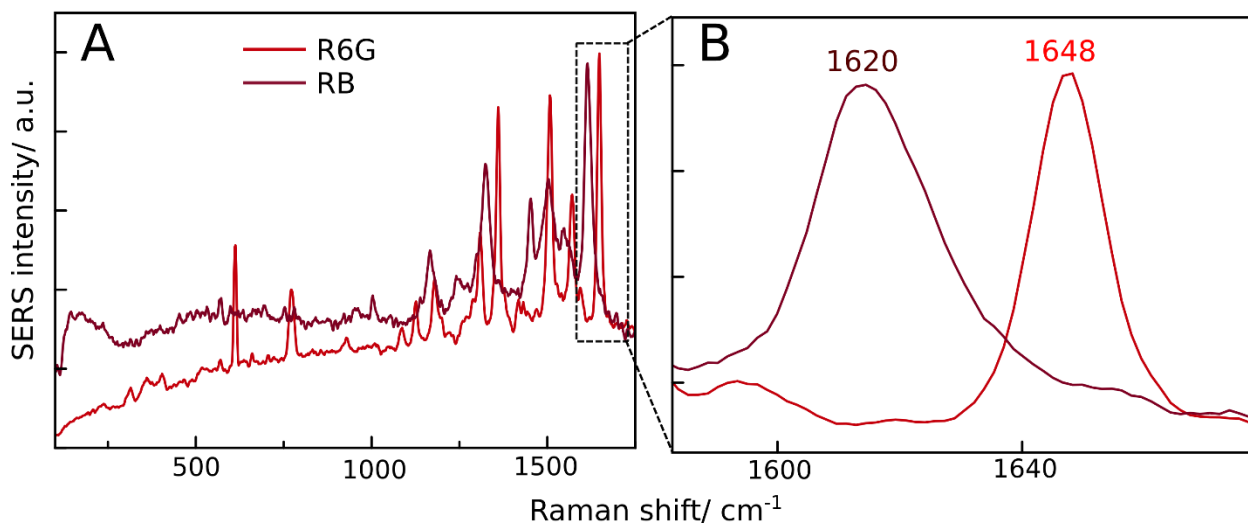

Figure 9. (A) 'Bulk' SERRS spectra of RB and R6G (100 nM). **(B)** Inset with the most intense SERS bands of RB and R6G, at 1620 and 1648 cm^{-1}, respectively.

As SERS marker bands for RB and R6G we chose their most intense SERRS peaks at 1620 and 1648 cm^{-1}, respectively, which will be further used for the statistical analysis of single molecule spectra.

Next, we prove the selectivity of RB and R6G adsorption on AgNPs at single molecule level, promoted by anionic and cationic adions, respectively. For this, we prepared two identical colloidal solutions containing both RB and R6G, the only difference being the type of adion added. From a total of 6000 spectra recorded, only 57 spectra contained a discernible SERS signal and were classified as single molecule events.

To analyze the SM-SERS events, we used the modified-PCA (MPCA) algorithm[4] based on the PCA, which extracts the main features in big datasets (in this case, the SERRS bands of RB and R6G), instead of relying only on the SERRS intensity of the 1620 and 1648 cm^{-1} bands. The PCA score plot of the SM-SERRS events (Figure 10A) is rotated based on the two vectors shown, representing the two dyes (R6G and RB) obtaining thus a new score plot (Figure 10B) in

which the vectors representing R6G and RB are now the coordinate basis vectors of the new space. The projection of any given point (corresponding to a SM-SERRS event) on the two coordinate vectors represents how much of the signal is from one molecule or the other.

The distribution found by our data (Figure 10C and D-F) is characteristic of SM-SERRS, suggesting to us that the SERRS signal comes indeed predominantly from single R6G molecules (on AgNPs@Cl$^-$) and single RB molecules (on AgNPs@Mg^{2+}).

Figure 10 shows the spectacular selectivity of SERS, obtained solely by using Cl$^-$ or Mg^{2+} adions. By adding Mg^{2+} to the colloidal AgNPs containing an RB/R6G mixture, the SERRS spectrum of RB can be observed at 1620 cm^{-1}, while by adding Cl$^-$ adions, only the SERS spectrum of R6G is observed, indicated by the 1648 cm^{-1} SERS band. In total, from 57 single molecule SERRS spectra on AgNPs@Cl$^-$ and AgNPs@Mg^{2+}, we only observed 15 mixed events (the blue bins in the histogram of Figure 10C) and no cross-event (i.e., no RB SERS events on AgNPs@Cl$^-$, and no R6G SERS event on AgNPs@Mg^{2+}), showing a remarkable selectivity.
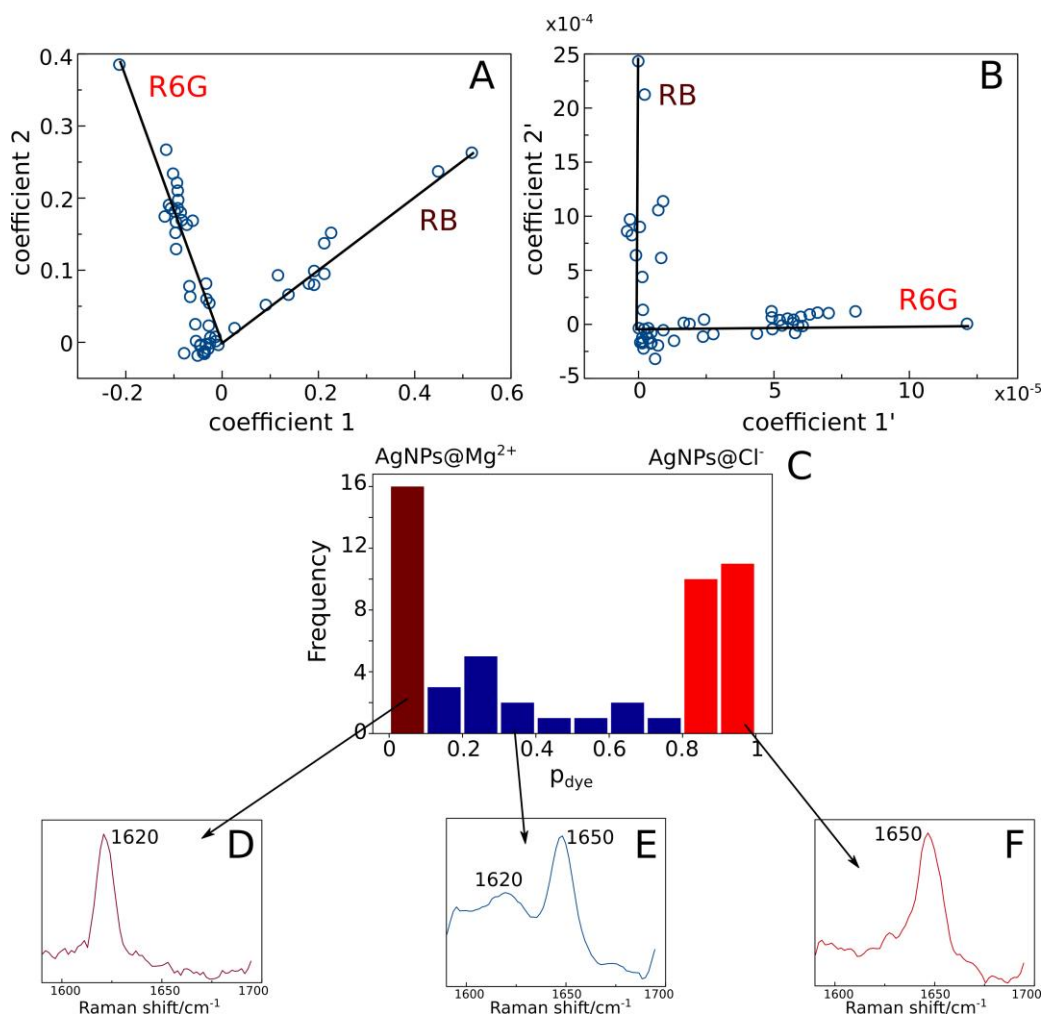
Figure 10. The statistical analysis of the 57 SM-SERRS events with the MPCA algorithm. **(A)** The score plot of the SM-SERRS events resulted from the PCA analysis, and the two vectors identified manually representing the R6G and RB SERRS signal. Each point in the score plot represents a SM-SERRS event. **(B)** The rotated score plot, so that the R6G and the RB vectors are now the coordinate basis vectors of the new space. **(C)** Histogram with the distribution of the SERRS events, characteristic to single molecule SERS spectra. Representative SM-SERRS events for **(D)** RB, **(E)** mixed and **(F)** R6G.

We show in this study the possibility to modulate the affinity of cationic and anionic molecules to the AgNPs surface at single molecule level by using anionic (i.e., Cl$^-$) and cationic (i.e., Mg^{2+}) adions, under the experimental parameters described here. This significantly increases the selectivity of SERS and could be used to solve the reproducibility issues in SERS. Moreover, to

the best of our knowledge, this is the first report showing single molecule SERS without adding Cl⁻, instead using Mg^{2+} which favor the adsorption of anionic species. Finally, we show some general trends in the adsorption of anionic species on AgNPs, which is a competitive process, and that of cationic species on AgNPs, which takes place cooperatively. We propose a physical mechanism in which Cl⁻ or Mg^{2+} adions bridge the specific adsorption (in the first layer) of cationic and anionic analytes respectively, in a selective manner, based on their charge.

Chapter IV. The effect of adsorbed halide ions in Fermi level equilibration

Chapter IV is based on the same physical-chemical mechanism as the one presented in Chapter II; namely, the upshift of the Fermi level of silver nanoparticles through the adsorption of halide ions, which leads to spontaneous charge transfer to adsorbed methylene blue molecules. The dynamic of the charge transfer, and of the methylene blue partial reduction to the intermediate radical form, HMB, was tracked in-situ, by SERS.

To track the energy level equilibration at the metal–molecule interface, we chose the reduction of MB^+ as a model system. MB^+ has a two steps electrochemical reduction pathway (Figure 11); the first one, to the intermediate form, $HMB^{+\bullet}$, takes place on Ag surfaces at a relatively low potential: –0.27 V (vs. Ag/AgCl); while the heterogeneous reduction to leuco methylene blue form (LMB) takes place at –0.365 V (vs. Ag/AgCl)[5]. Notably, the conformational and structural changes in the MB^+ molecules can be easily tracked by SERS, allowing us to identify with great specificity and sensitivity the reduction of MB^+ on the surface of AgNPs (Figure 11, B-D). Through the reduction of MB^+ to the intermediate radical $HMB^{+\bullet}$ and LMB forms, respectively, the molecular optical resonance shifts further away from the visible to the UV range. The absorbance maxima of MB^+ at 662 and 610 nm (corresponding to the monomer and dimer forms[5]) shifts to 410 and 880 nm for the $HMB^{+\bullet}$ form and finally to 325 nm for the LMB form.

To probe the SERS features of each MB^+ form (i.e. MB^+, $HMB^{+\bullet}$ and LMB), we used a highly potent reducing agent, $NaBH_4$, which was shown to fully reduce MB^+. The molecular structure changes upon reduction of MB^+ to the $HMB^{+\bullet}$ and LMB forms can be tracked by SERS. In particular, the newly formed N-H bond in both MB^+ reduction products, $HMB^{+\bullet}$ and LMB, is observed. The SERS bending N-H mode was reported at 1160 cm⁻¹ for imidazole and at 1121 cm⁻¹ for pyrazole. Therefore, the features at ~1130 cm⁻¹, observed in the SERS spectra of the

HMB$^{+\bullet}$ form was assigned to the N-H bending mode. The reduction of MB^{+} to HMB$^{+\bullet}$ leads to a gradual loss in the molecular aromaticity most likely because of a decrease in the p orbital overlap between C, N and S atoms in the thiazine ring. Moreover, the presence of an N-H bond and the breaking of the double bond in the aromatic ring of the HMB$^{+\bullet}$ contributes to the loss of aromaticity. Consequently, the bond order involving the C-N-C and C-S-C moieties should decrease, leading to a shift to lower wavenumbers of their Raman vibrational modes. In Figure 11 B, C, and D, it can be observed that the spectral features at 1622, 1395, 1070 and 1040 cm^{-1} in the SERS spectra of MB^{+} are shifted to lower wavenumbers in the SERS spectra of HMB$^{+\bullet}$. Additionally, a new SERS band at 1500 cm^{-1} appears in the intermediate, HMB$^{+\bullet}$ form. For the LMB form, the SERS intensity decreases drastically (Figure 11B), due to the loss of resonance in the visible part of electromagnetic spectrum.
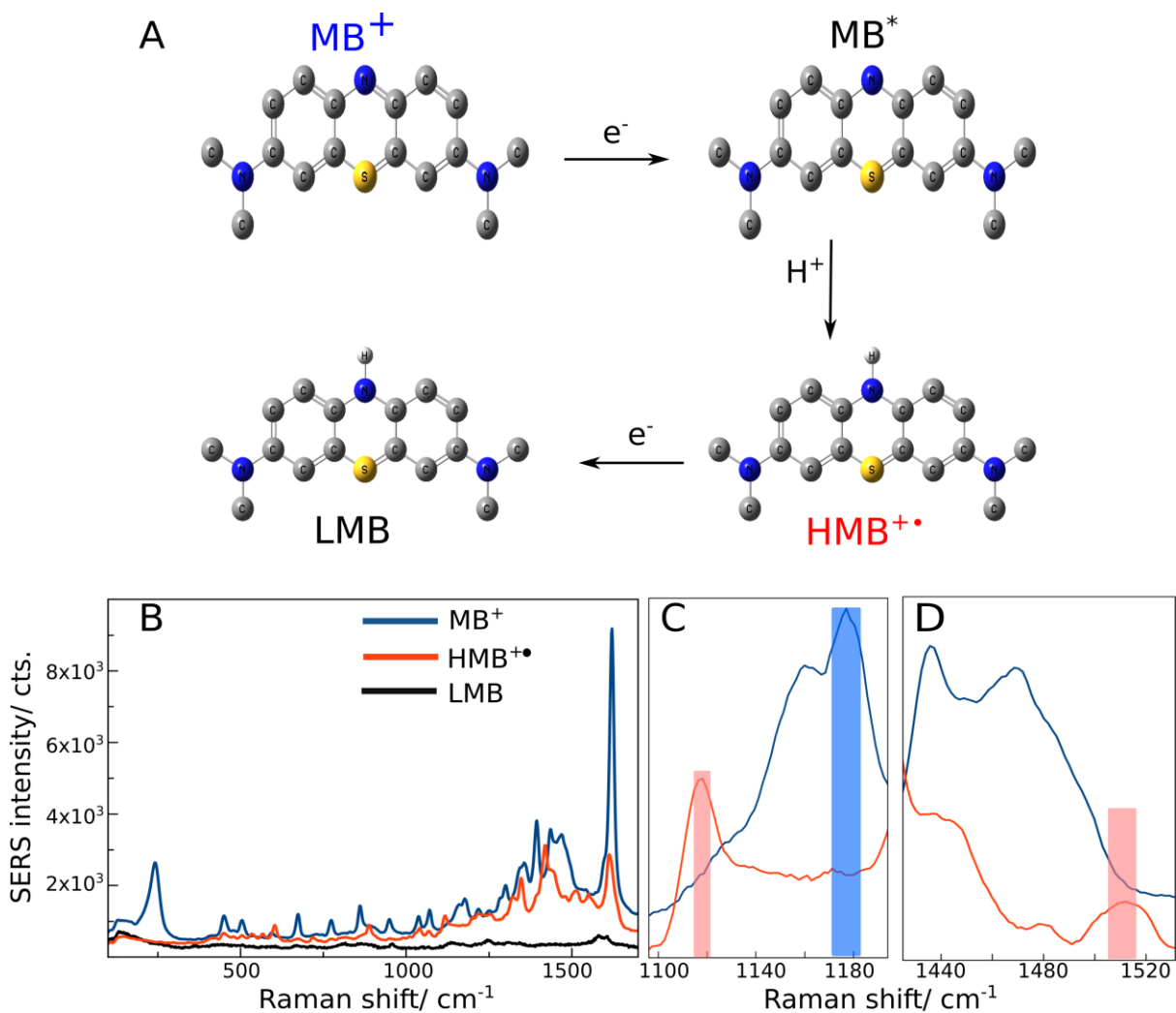
Figure 11. (A) The two-step reduction scheme of MB^+ to the first unstable intermediate form (MB*), to the radical intermediate form ($HMB^{+\bullet}$) and to the fully reduced form (LMB). **(B)** SERS spectra of MB^+, $HMB^{+\bullet}$ and LMB forms during the AgNPs-catalyzed reduction of MB^+ by $NaBH_4$, acquired with 532 nm excitation. **(C)** The appearance of the N-H bending mode on the intermediate $HMB^{+\bullet}$ form at 1130 cm^{-1} and **(D)** C-C stretching mode of the thiazine ring at 1510 cm^{-1} in the SERS spectrum of $HMB^{+\bullet}$.

Figure 12 shows the formation of $HMB^{+\bullet}$ species on the surface of AgNPs@Br and AgNPs@I, tracked by SERS. The ratio of $HMB^{+\bullet}/MB^+$ on the AgNPs surface can be followed qualitatively using the 1150/1180 cm^{-1} SERS intensity ratio (Figure 12 A, B, E). It has to be mentioned that the MB^+ and $HMB^{+\bullet}$ forms have different SERS cross-sections, thus the 1150/1180 cm^{-1} intensity ratio does not correspond to an absolute quantitative ratio of the two molecular species. Rather, it shows the relative, qualitative difference in the concentration difference of $HMB^{+\bullet}$ form on AgNPs@Cl, AgNPs@Br and AgNPs@I.

Figure 12B shows the SERS bands at 1150 (from the N-H bond of $HMB^{+\bullet}$) and 1180 cm^{-1} (from the MB^+) on AgNPs@Cl, AgNPs@Br and AgNPs@I. Thus, by taking their relative ratio, we can infer semi-quantitatively the ratio of the two molecular forms on the three different Ag surfaces (Figure 12E). To correlate the $HMB^{+\bullet}/MB^+$ ratio with the Fermi level upshift on AgNPs@Br and AgNPs@I, we plotted the 1150/1180 cm^{-1} SERS intensity (i.e., % of conversion) against the DFT calculated Fermi level of the three surfaces AgNPs@Cl, AgNPs@Br and AgNPs@I (on the x-axis) (Figure 12E).
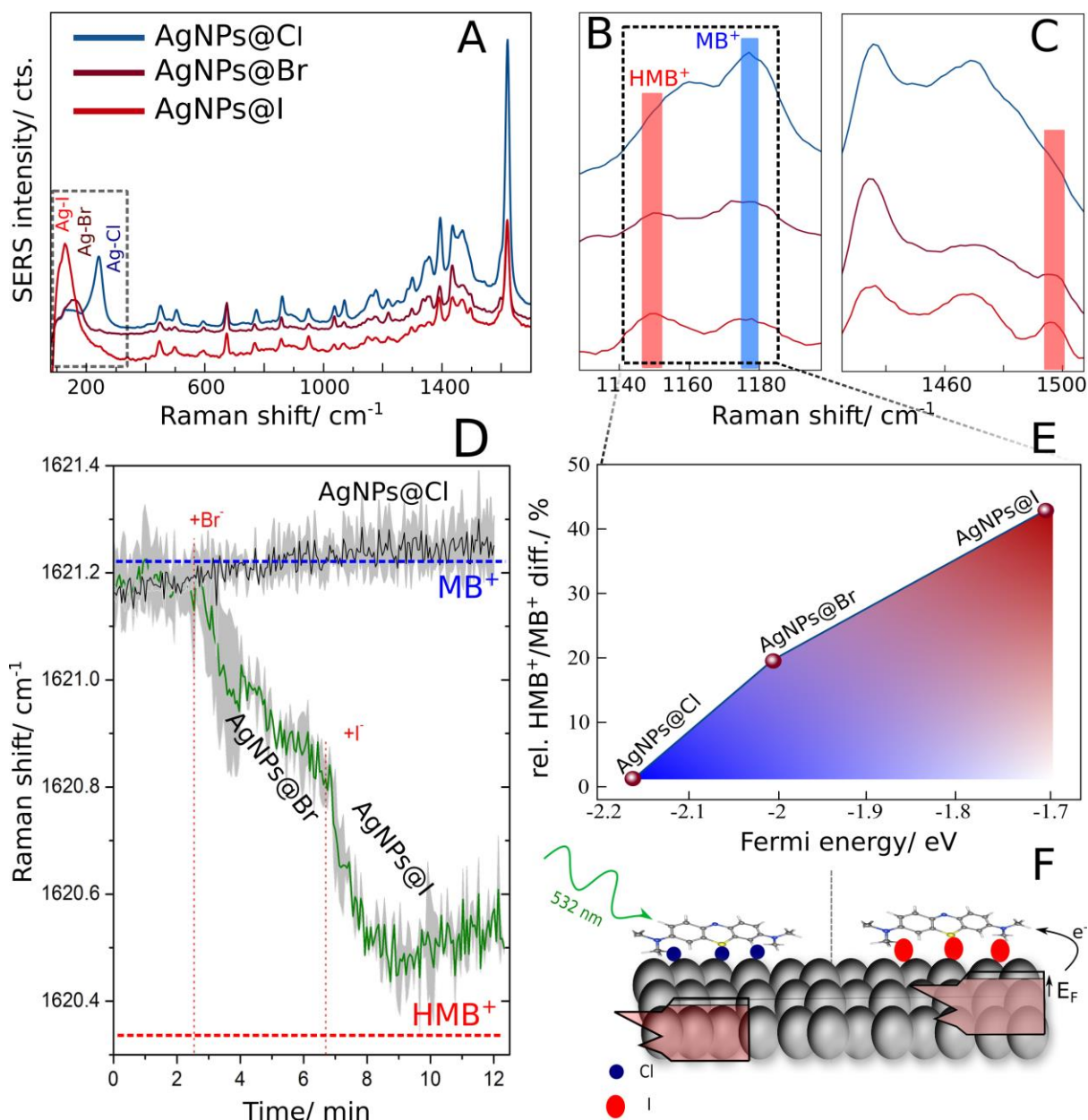
Figure 12. The reduction of MB$^+$ on the surface of AgNPs, due to the shift of the Fermi level, monitored with 532 nm excitation. **(A)** SERS spectra of MB$^+$ on AgNPs@Cl, AgNPs@Br and AgNPs@I. The low wavenumber region shows the surface dynamics of Cl$^-$ (240 cm^{-1}), Br$^-$ (160 cm^{-1}) and I$^-$ (130 cm^{-1}). **(B-C)** Insets from (A), showing the spectral changes characteristic to HMB$^{+\bullet}$ that appear after the adsorption of Br$^-$ and especially I$^-$. **(D)** Time-series SERS measurements of MB$^+$ on AgNPs@Cl, modifying, *in-situ*, the surface of AgNPs with Br$^-$ and I$^-$ (10 μM), at the marked times. After the sequential addition of Br$^-$ and I$^-$, the SERS peak at 1621 cm^{-1} shifts to lower wavenumbers, characteristic to HMB$^{+\bullet}$. **(E)** The relative percentual increase

in the 1150/1180 cm^{-1} SERS intensity ratio corresponding to the HMB$^{+\bullet}$/ MB^{+} ratio on the surface of AgNPs@Cl, AgNPs@Br and AgNPs@I from (B) plotted against the Fermi level energies determined from the DFT calculations, on the x-axis. **(F)** Schematic representation of the reduction of MB^{+} on the surface of AgNPs, due to the shift of Fermi level after the chemisorption of I^{-}. Analogous to electrochemistry experiments, the Fermi level of AgNPs is raised, favoring the *spontaneous* electron transfer across the interface to the unoccupied level of adsorbed MB^{+}.

Importantly, the Ag-halide SERS band at low wavenumbers allow us to monitor the surface dynamics of halide ions and MB^{+} in real time, gaining thus a mechanistic understanding on the elusive role of halides in SERS and plasmonic chemistry (Figure 12A). Monitoring the surface dynamics of halides through their specific SERS bands is quite uncommon, since most studies focus on the fingerprint region, usually from 500 to 1800 cm^{-1}, and therefore they track the effect of halide ligands indirectly, only through changes in the SERS spectra of the probe molecule.

Taking advantage of the possibility of tracking *in-situ* the surface dynamics of halide ions and MB^{+}, we monitored the exchange of halide ions on the surface of AgNPs, and the consequent reduction of MB^{+} (Figure 12D). This time, we chose as a SERS marker band for the reduction of MB^{+} the down shift of the 1621 cm^{-1} band, which stems from the systematic loss of aromaticity of MB^{+} upon reduction (see Figure 11B). At t = 0, MB^{+} is chemisorbed on AgNPs@Cl, the MB^{+} adsorption being mediated by Cl^{-}. At t = 2.5 min, KBr was added to the colloidal solution and the Br^{-} ions replace Cl^{-} ions on the surface of the AgNPs due to their higher affinity. Adsorbed Br^{-} ions raise the Fermi energy of AgNPs and, consequently, promote the charge transfer from the Fermi energy to the unoccupied orbital of adsorbed MB^{+}, forming HMB$^{+\bullet}$. At t = 6 min and 45 s, KI is added to the colloidal solution. I^{-} ions displace Br^{-} ions from the surface of AgNPs due to their higher affinity. As in the case of Br^{-}, the Fermi energy is further raised, promoting an even higher rate of charge transfer from the Fermi level to the LUMO orbital of MB^{+} until the energy levels are equilibrated, as evidenced by the plateau reached at the end of the measurement (10– 12 min). Solely in the presence of Cl^{-}, the 1621 cm^{-1} band shifts insignificantly (Figure 12D), proving that the reduction of MB^{+} is thermodynamically driven by the equilibration in the energy

levels of the AgNPs–MB$^+$ system, and not due to the photoexcitation of electrons from the AgNPs upon 532 nm excitation.

The decrease in intensity of MB$^+$ SERS bands as Br$^-$ and I$^-$ are added, observed in Figure 12A, is attributed to the partial reduction of MB$^+$ to the less radiative form HMB$^{+\bullet}$. This is also observed in Figure 12B, most notably for the 1621 cm^{-1} SERS band, as reported previously

In conclusion, we have shown that the role of halide ions in the metal–molecule charge transfer process is dictated by the adsorption regime of the halide ions. Through the chemisorption of halide ions, Ag-X (X= Cl, Br, I) surface complexes form, which alter the surface potential and the Fermi energy of the AgNPs. This, in turn, can lead to spontaneous metal-molecule charge transfer if the acceptor orbitals of the adsorbed molecule are properly aligned with the Fermi level of the metal, as in the AgNPs-MB case. Our results show that in some cases the effect of adsorbed ions on plasmonic nanomaterials can be energetically comparable (~0.3 eV) with the light-induce surface voltage effect (photovoltage) or the energy of hot-carriers participating in catalytic processes.

However, when the metal surface is occupied with molecules with a stronger affinity for the metal surface than halide ions, particularly thiolated molecules, the halide ions cannot co-adsorb on the surface, which can be readily checked experimentally through the Ag-halide SERS bands (also valid for Au NPs). Thus, their role in the metal-molecule charge transfer is a "transient" one, in the sense that they do not modify directly the catalytic and electronic properties of metal NPs, but they scavenge the hot holes created through SPR excitations or inter- and intraband transitions. In summary, these results highlight the important and many times underestimated role of capping agents, electric double layer, reaction media and halides co-adsorption in plasmonic catalysis and surface enhanced spectroscopies.

Chapter V. The effect of adsorbed halide ions in changing the optical properties of adsorbed molecules

Finally, **Chapter V** demonstrates how the chemical nature of the metal-molecule interface can have surprising effects on the electron dynamics of the entire complex. Particularly, for excited,

adsorbed rhodamine 6g and crystal violet molecules, the non-radiative decay rate increases in the sequence: AgNPs@Cl<AgNPs@Br<AgNPs@I. Moreover, the chemical interface damping of the AgNPs with the halide ions follows the same trend. These results can be explained by the formation of metal-halide surface complexes, which can accept electrons, transiently, from both excited molecules, and from the surface plasmon resonance.

The average SM-SERS spectra of CV (Figure 13B) clearly show a decrease in the SEF emission of CV on AgNPs@Br and AgNPs@I compared to AgNPs@Cl, consistent throughout all measurements. This suggests an increase in the non-radiative decay rate (i.e., relaxation of CV by energy transfer to AgNPs instead of emitting a Stokes-shifted photon). Based on this observation, we aimed to quantify the changes in the radiative and non-radiative decay rates of CV on the three metal surfaces: AgNPs@Cl, AgNPs@Br and AgNPs@I.

Figure 13A shows the Raman spectrum of a CV solution (1 mM) taken in the same experimental conditions as the SM-SERS spectra (average spectra presented in Figure 13B) and illustrates the methodology for obtaining the radiative and non-radiative decay rates of CV from its Raman and SM-SERS spectra, adapted from the work of Galloway et. al. [6]

The ratio, R_{Bare} (R_{AgNP}), of Raman (SERS) to fluorescence (SEF) signal is extracted for four Raman bands of CV (i.e., 799, 1170, 1385 and 1616 cm^{-1}). Then, the ratio of R_{AgNP} to R_{Bare} is computed for each of the four Raman bands. This method has the advantages that is self-normalizing, since it is based not on the ratio of SERS and SEF intensities but on the ratio of the Raman and fluorescence enhancement factors, and is not sensitive to photobleaching of the dye.

This method of extracting the radiative and non-radiative decay rates can be applied to CV, since CV is one of the few dyes with a low enough quantum yield, 5.2×10^{-5}, to allow its direct resonant Raman detection. For most other dyes, their high quantum yield leads to the complete cover of Raman peaks in the broad fluorescence emission.
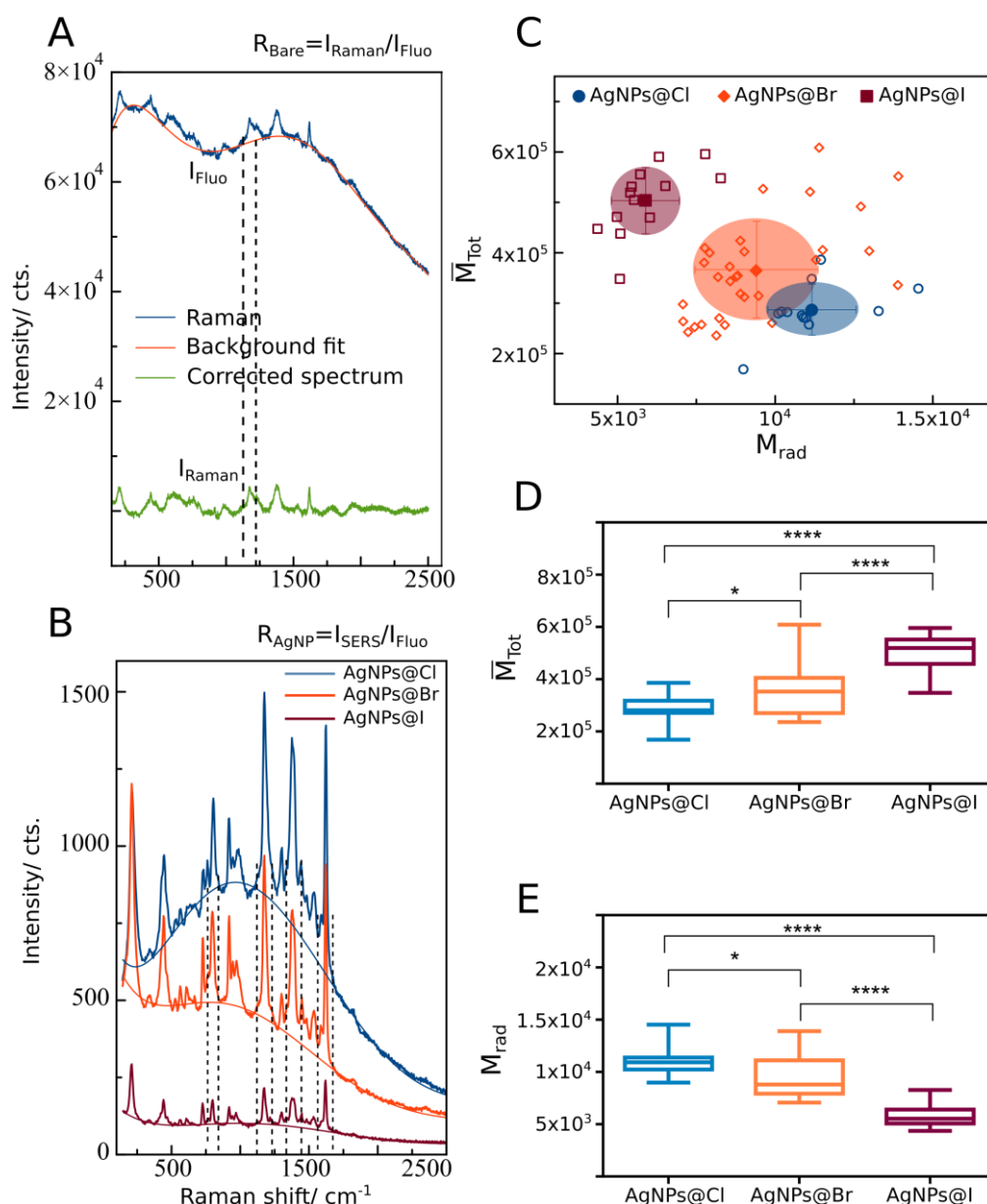
Figure 13. Resonant Raman and SM-SERS spectra of CV used to calculate the decay rate of CV. **(A)** Resonant Raman spectrum of a 1 mM solution of CV. The spectrum was background corrected to extract the fluorescence and Raman intensities. From the Raman and fluorescence intensities, the ratio R_{Bare} is computed for the 799, 1170, 1385 and 1616 cm^{-1} peaks. **(B)** The average SM-SERS spectra of CV obtained on AgNPs@Cl, AgNPs@Br and AgNPs@I. From the background corrected SM-SERS spectrum, the SERS and SEF intensities are extracted and used to compute R_{AgNP} for the same four peaks as in the Raman spectrum. **(C)** The total decay rate, $\overline{M}_{Tot}$, of CV adsorbed on AgNPs@Cl, AgNPs@Br and AgNPs@I, plotted against the radiative

decay rate, M_{rad}. Each point in the figure represents the $\overline{M}_{Tot}$ and M_{rad} obtained from one SM-SERS spectrum of CV on AgNPs@Cl, AgNPs@Br and AgNPs@I, respectively. The shaded regions represent the 2-dimensional standard deviations. **(D-E)** The statistical significance of the change of $\overline{M}_{Tot}$ and M_{rad}, respectively, on AgNPs@Cl, AgNPs@Br and AgNPs@I. The normality of the distribution was checked by D'Agostino and Pearson omnibus normality test and the significance was assessed by one-way ANOVA test ($*= p < 0.5; ****= p < 0.001$).

We show in the present study the intricate relation between the adsorption of halide ions on AgNPs and the plasmon-assisted optical processes on the surface of AgNPs. Particularly, through SM-SERS measurements we show that Br⁻ and I⁻ lead to an increase in the total decay rate of excited, adsorbed CV and R6G by a factor of ~3, compared to AgNPs@Cl, while the radiative decay rate remains approximately constant on all three metal surfaces (AgNPs@Cl, AgNPs@Br and AgNPs@I). Moreover, we found that the CID (plasmon resonance decay into surface states) is stronger on AgNPs@Br and AgNPs@I compared to AgNPs@Cl, both effects (increase of the total decay rate and CID) following the same trend: Cl⁻<Br⁻<I⁻.

Although the changes in the total decay rate of adsorbed CV and R6G could be explained by a decrease in the metal-molecule separation, favoring the interaction of molecular transitions with higher-order, non-radiative, plasmon modes, we propose an alternative mechanism which explains both the CID trend and the variations in the total decay rate. We hypothesize the formation of hybrid (Ag-halide)⁺ energy states which can accept electrons, either from the plasmon resonance, explaining the increase in CID, or from the molecular orbitals, explaining the total decay rate increase of excited CV and R6G. This mechanism is additionally supported by the SERS intensity of the Ag-halide bands, measured on solid Ag SERS substrates, which follows the same sequence as the CID: Ag-Cl<Ag-Br<Ag-I. We attribute this intensity increase to a chemical enhancement of the Raman signal of Ag-X bands (X=Cl⁻, Br⁻, I⁻), which is most pronounced for the Ag-I surface complexes, that have the highest electron-accepting character.

References

1.	Le Ru, E. C.; Etchegoin, P. G., *Principles of surface-enhanced raman spectroscopy : and related plasmonic effects*. Elsevier: Amsterdam; Heidelberg, 2011.

2.	Johnson, P. B.; Christy, R. W., Optical Constants of the Noble Metals. *Physical Review B* **1972,** *6* (12), 4370-4379.

3.	Linnert, T.; Mulvaney, P.; Henglein, A., Surface chemistry of colloidal silver: surface plasmon damping by chemisorbed iodide, hydrosulfide (SH-), and phenylthiolate. *The Journal of Physical Chemistry* **1993,** *97* (3), 679-682.

4.	Etchegoin, P. G.; Meyer, M.; Blackie, E.; Le Ru, E. C., Statistics of Single-Molecule Surface Enhanced Raman Scattering Signals: Fluctuation Analysis with Multiple Analyte Techniques. *Analytical Chemistry* **2007,** *79* (21), 8411-8415.

5.	Nicolai, S. l. H. d. A.; Rodrigues, P. R. P.; Agostinho, S. M. L.; Rubim, J. C., Electrochemical and spectroelectrochemical (SERS) studies of the reduction of methylene blue on a silver electrode. *Journal of Electroanalytical Chemistry* **2002,** *527* (1), 103-111.

6.	Galloway, C. M.; Etchegoin, P. G.; Le Ru, E. C., Ultrafast Nonradiative Decay Rates on Metallic Surfaces by Comparing Surface-Enhanced Raman and Fluorescence Signals of Single Molecules. *Physical Review Letters* **2009,** *103* (6), 063003.